# Hidden ferronematic order in underdoped cuprates

G. Seibold,[1] M. Capati,[2] C. Di Castro,[2] M. Grilli,[2] and J. Lorenzana[2]
[1]*Institut für Physik, BTU Cottbus, P.O. Box 101344, 03013 Cottbus, Germany*
[2]*ISC-CNR, CNISM, and Dipartimento di Fisica, Università di Roma "La Sapienza", Piazzale Aldo Moro 5, I-00185 Roma, Italy*
(Received 10 April 2012; revised manuscript received 17 January 2013; published 30 January 2013; publisher error corrected 4 February 2013)

We study a model for low-doped cuprates where holes aggregate into oriented stripe segments which have a magnetic vortex and antivortex at the extremes. We argue that due to the interaction between segments a ferronematic state with macroscopic polarization is stabilized. This state can be characterized as a charge nematic which, due to the net polarization, breaks inversion symmetry and also exhibits an incommensurate spin modulation. Our calculation can reproduce the doping-dependent spin structure factor of lanthanum cuprates in excellent agreement with experiment and allows to rationalize experiments in which the incommensurability has an order-parameter-like temperature dependence.

DOI: 10.1103/PhysRevB.87.035138 PACS number(s): 74.25.Ha, 71.28.+d, 74.72.−h, 75.25.−j

## I. INTRODUCTION

The question of whether there is a broken-symmetry hidden order in the pseudogap phase of cuprate high-temperature superconductors is still a matter of debate. Proposals for a broken-symmetry state include orbital currents which break time-reversal symmetry,[1] spirals,[2] $d$-density wave,[3,4] and $d$-wave Pomeranchuk Fermi surface instability.[5] In this regard, a popular proposal is the formation of stripes which corresponds to unidirectional charge[6,7] or spin and charge order[8,9] eventually supplemented with a modulation of superconducting order.[10]

Bulk evidence for charge stripe order in the high-temperature superconductors has so far only been found in $La_{1.875}Ba_{0.125}CuO_4$[11] and $La_{1.8-x}Eu_{0.2}Sr_xCuO_4$[12] by resonant soft x-ray scattering experiments. Similarly to the compound $La_{1.48}Nd_{0.4}Sr_{0.12}CuO_4$, where the phenomenon of stripe formation has been initially seen via the coupling of the charge order to the lattice,[13] these materials undergo a low-temperature tetragonal lattice (LTT) distortion which pins charge order along the copper-oxygen bond direction. The coupling of charge with the longitudinal spin component then induces a concomitant modulation in the spin channel which within neutron scattering can be detected as an elastic or low-energy incommensurate response. Recently the direct occurrence of charge density waves has been observed by resonant x-ray scattering[14,15] also in YBCO materials around 1/8 doping. Low-energy incommensurate spin scattering is also found in non-codoped lanthanum cuprates, where it undergoes a rotation toward the diagonal direction below hole concentrations $x \lesssim 0.05$ where it even becomes elastic.[16–18] No charge order, however, has been observed so far at low doping. Interestingly the incommensurability $\delta$ (proportional to the inverse of the spin modulation) evolves linearly $\delta \sim x$ from $x = 0.02$ up to the metallic (or SC below $T_c$) phase where it saturates above $x \gtrsim 1/8$.[19] Below $x \approx 0.02$ commensurate antiferromagnetic order coexists with a spin-glass phase with incommensurate spin correlations.[20] It is also worth mentioning that a recent inelastic neutron scattering study of single-layer $Bi_{2+x}Sr_{2-x}CuO_{6+y}$ (Bi2201) cuprates[21] has revealed the same incommensurability of low-energy spin fluctuations as for LSCO.

Quasistatic incommensurate spin scattering along the Cu-O bond direction has also been found in detwinned YBCO.[22,23] This also raised the issue of the melting of this order and of the possibility of (dynamical) precursors of such order. In any case, the experimental evidence of rotational symmetry breaking[22–24] points towards a nematic order although it is not yet clear whether this order arises from a melted stripe state,[25] from incipient unidirectional fluctuating stripes,[26] or from an independent $d$-wave type nematic actor which preserves translational symmetry.[27]

In this paper we show that neutron scattering experiments in strongly underdoped cuprates can be understood in terms of a phase which breaks rotational *and* inversion symmetry. It is formed by oriented stripe segments without positional order that leads to ferronematic order. A ferronematic state can arise also in the Fermi liquid in the presence of long-range dipolar forces.[28] The segments are oriented because they sustain a vortex and an antivortex of the antiferromagnetic (AF) order in the extremes (Fig. 1). Although the phase has no order in the charge sector, we show that it induces magnetic incommensurate peaks in excellent agreement with experiments (Fig. 8). Remarkably, the order parameter is proportional to the incommensurability as suggested by neutron scattering measurements.[22,23] We focus on nonsuperconducting underdoped LSCO which can be grown in a structure with only two twin domains with different population. Therefore, similarly to the case of YBCO, the one-dimensionality of the low-energy (diagonal) spin response can be clearly resolved.[17,18]

The structure of the paper is as follows: In Sec. II we introduce the microscopic electronic model and give the details of its solution. In Sec. III we present the variational results showing the formation of charge segments, while in Sec. IV we describe the effects of the long-range Coulombic repulsion limiting the length of the segments. Section V describes the mapping of the microscopic electronic model to the pure spin model and the related formation of spin-phase regions responsible for the incommensurate spin response. The comparison with the experimental neutron scattering intensity is also reported here. The discussion of the results and our concluding remarks are in Sec. VI.

## II. MODEL AND CALCULATION METHODS

For the (low) doping spin structure, previous variational computations[29–32] in cuprates suggest the formation of

 

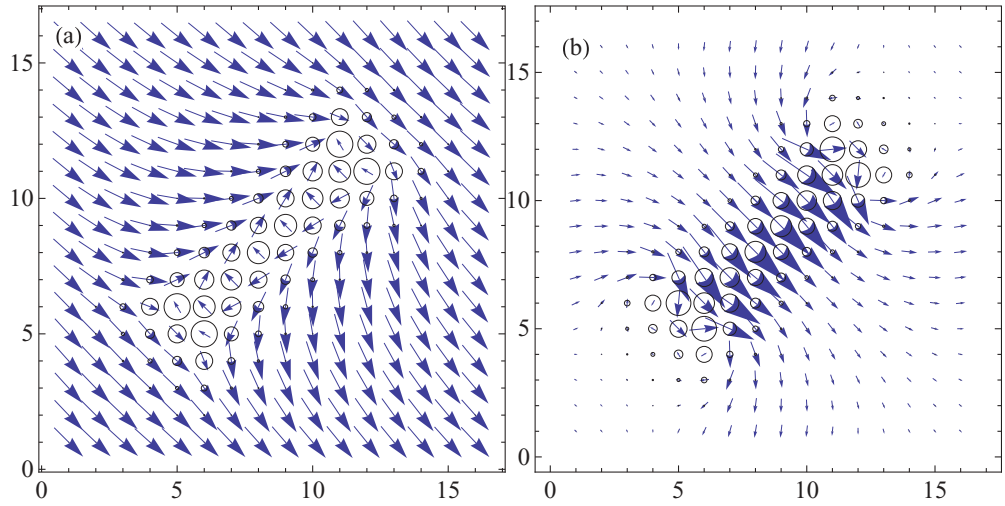


FIG. 1. (Color online) (a) Stripe segment for $N_c = 8$ added holes (corresponding to 4 VA pairs) obtained by minimizing the GA energy on a $16 \times 16$ lattice in the one-band Hubbard models with $t'/t = -0.2$. The radius of the circles is proportional to the added hole density while the arrows are the staggered magnetization. (b) Spin currents [Eq. (5)] defined from the conservation of the $z$ component of the magnetization. In the continuum limit the spin current is proportional to the gradient of the phase of the staggered magnetization.

magnetic vortex-antivortex (VA) pairs, the relevance of which has been discussed, e.g., in the context of the destruction of long-range Néel order.[33] In order to study these textures we have performed variational calculations based on the Gutzwiller approximation (GA) of the extended one-band Hubbard model (see Ref. 30 for details of the approach)

$$H = \sum_{i,j,\sigma} t_{ij} c^{\dagger}_{i,\sigma} c_{j,\sigma} + U \sum_{i} n_{i,\uparrow} n_{i,\downarrow}, \tag{1}$$

where $c_{i,\sigma}$ ($c^{\dagger}_{i,\sigma}$) destroys (creates) an electron with spin $\sigma$ at the site $i$, and $n_{i,\sigma} = c^{\dagger}_{i,\sigma} c_{i,\sigma}$ is the number operator at the site $i$. $U$ is the on-site Hubbard repulsion and $t_{ij}$ denotes the hopping parameter between sites $i$ and $j$. We restrict our attention to hopping between nearest ($\sim t$) and next-nearest ($\sim t'$) neighbors. We base our calculations on the Gutzwiller variational wave function $|\Psi_g\rangle = P_g|\mathrm{SD}\rangle$, where $P_g$ is the Gutzwiller projector and $|\mathrm{SD}\rangle$ a Slater determinant. For $|\mathrm{SD}\rangle$ we use a state with arbitrary charge and spin order, including spin canting. This limits our calculations to clusters of $20 \times 20$ sites. We define the associated one-body density as $\rho_{ij}^{\sigma_1,\sigma_2} = \langle \mathrm{SD}|c^{\dagger}_{j\sigma_2} c_{i\sigma_1}|\mathrm{SD}\rangle$. The wave-function optimization problem leads to a generalized Gutzwiller approximation,[34] which on the saddle-point level is equivalent to the Kotliar-Ruckenstein slave-boson approach.[35] The derivation of the spin-rotational-invariant Gutzwiller energy functional can be found in Ref. 36:

$$E^{GA} = \sum_{i,j} t_{ij} \langle \Psi_i^{\dagger} \mathbf{z}_i \mathbf{z}_j \Psi_j \rangle + U \sum_{i} D_i. \tag{2}$$

Here we have defined the spinor operators

$$\Psi_i^{\dagger} = (c^{\dagger}_{i,\uparrow}, c^{\dagger}_{i,\downarrow}), \qquad \Psi_i = \begin{pmatrix} c_{i,\uparrow} \\ c_{i,\downarrow} \end{pmatrix}$$

and the $\mathbf{z}$ matrix

$$\mathbf{z}_i = \begin{pmatrix} z_{i\uparrow} \cos^2 \frac{\varphi_i}{2} + z_{i,\downarrow} \sin^2 \frac{\varphi_i}{2} & \frac{S_i^-}{2S_i^z}[z_{i\uparrow} - z_{i\downarrow}] \cos \varphi_i \\ \frac{S_i^+}{2S_i^z}[z_{i\uparrow} - z_{i\downarrow}] \cos \varphi_i & z_{i,\uparrow} \sin^2 \frac{\varphi_i}{2} + z_{i\downarrow} \cos^2 \frac{\varphi_i}{2} \end{pmatrix}, \quad \tan^2 \varphi_i = \frac{S_i^+ S_i^-}{\left(S_i^z\right)^2},$$

and for clarity the spin expectation values in the Slater determinant are denoted by $S_i^+ = \rho_{ii}^{\uparrow,\downarrow}$, $S_i^- = \rho_{ii}^{\downarrow,\uparrow}$, $S_i^z = (\rho_{ii}^{\uparrow,\uparrow} - \rho_{ii}^{\downarrow,\downarrow})/2$, and $\rho_{ii} = \rho_{ii}^{\uparrow,\uparrow} + \rho_{ii}^{\downarrow,\downarrow}$. In the limit of a vanishing rotation angle $\varphi$ the $\mathbf{z}$ matrix becomes diagonal and the renormalization factors

$$z_{i\sigma} = \frac{\sqrt{(1 - \rho_i + D_i)\left(\frac{1}{2}\rho_i + \frac{S_i^z}{\cos(\varphi_i)} - D_i\right)} + \sqrt{D_i\left(\frac{1}{2}\rho_i - \frac{S_i^z}{\cos(\varphi_i)} - D_i\right)}}{\sqrt{\left(\frac{1}{2}\rho_i + \frac{S_i^z}{\cos(\varphi_i)}\right)\left(1 - \frac{1}{2}\rho_i - \frac{S_i^z}{\cos(\varphi_i)}\right)}}$$

reduce to those of the standard GA. Variational solutions are computed by minimizing $E^{GA}$ with respect to the Slater determinant and to the local double occupancy $D_i$.

In the following the ratio between on-site repulsion $U$ and nearest-neighbor hopping $t$ is set to $U/t = 8$ as suggested by previous studies.[37,38] The ratio between

next-nearest-neighbor hopping $t'$ and $t$ is taken as a material parameter.[39,40]

The spin textures in the present papers are conveniently characterized by the associated spin currents (see Fig. 1) flowing from site $R_i$ to $R_j$. These are defined via the continuity equation

$$\partial_t S_i^\alpha + \sum_j J_{i\to j}^\alpha = 0, \tag{3}$$

where $\sum_j J_{i\to j}^\alpha$ is the generalized lattice divergence of the $\alpha$ component of the local spin current at site $R_i$.

Together with the Heisenberg equation of motion $\partial_t S_i^\alpha = i[H, S_i^\alpha]$ one thus finds

$$\sum_j J_{i\to j}^\alpha = -i\big[H, S_i^\alpha\big]. \tag{4}$$

Evaluating the expectation value of Eq. (4) within the GA yields

$$J_{i\to j}^{GA,\alpha} = t_{ij}\, Im \sum_{\sigma_1\ldots\sigma_4} \sum_{k=1}^{N_{el}} \Phi_{i\sigma_1}^*(k)\tau_{\sigma_1\sigma_2}^\alpha z_{i\sigma_2,\sigma_2} z_{j\sigma_4\sigma_3} \Phi_{j\sigma_4}(k), \tag{5}$$

where $\Phi_{i,\sigma_1}(k)$ are the amplitudes which diagonalize the Gutzwiller Hamiltonian and $\tau_{\sigma_1\sigma_2}^\alpha$ denote the Pauli matrices.

## III. VARIATIONAL RESULTS

Within this variational framework the energetically most stable solution for two holes is a VA pair.[30] Specifically, a single hole deforms the AF background and can be viewed as a self-trapped spin polaron, while two holes have lower energy as a VA pair rather than two independent spin polarons. The VA pair has a magnetic dipole $\boldsymbol{\mu} = k\mathbf{l}$, $k$ being the vorticity and $\mathbf{l}$ the vector connecting V and A. The theory which is developed in the following is precisely based on the tendency of doped holes in an AF background to form a gas of VA pairs. These adopt the role of dipole particles in dipolar fluids.[41] The individual pairs interact via a two-dimensional dipole-dipole interaction

$$V_{\rm mag} = \frac{\boldsymbol{\mu}_1\boldsymbol{\mu}_2}{\mathbf{R}^2} - 2\frac{(\boldsymbol{\mu}_1\mathbf{R})(\boldsymbol{\mu}_2\mathbf{R})}{\mathbf{R}^4}, \tag{6}$$

where $\mathbf{R}$ connects the center of the two pairs (see insets of Fig. 2).

Contrary to the 3D case, for the 2D dipole-dipole interaction the head-to-tail alignment and the side-by-side quadrupolar configurations in the insets of Fig. 2 are energetically degenerate. However, our GA computations reveal the presence of an anisotropic short-range contribution for the interaction among pairs, which originates from the distribution of the localized holes. This results in a head-to-tail aggregation of VA pairs which tend to form chains with a dipolar like distortion of the AF background (see Fig. 2). Figure 1(a) shows the spin and charge structure for 8 holes corresponding to 4 VA pairs. Examination of the spin current, Fig. 1(b), allows one to visualize the VA pair nucleated at the extremes of the segment and the fact that the texture breaks inversion symmetry. Notice that the segments tend to form an antiphase domain wall of the AF order although the transition from finite segments to infinite stripes is nontrivial and will be discussed elsewhere.[42]

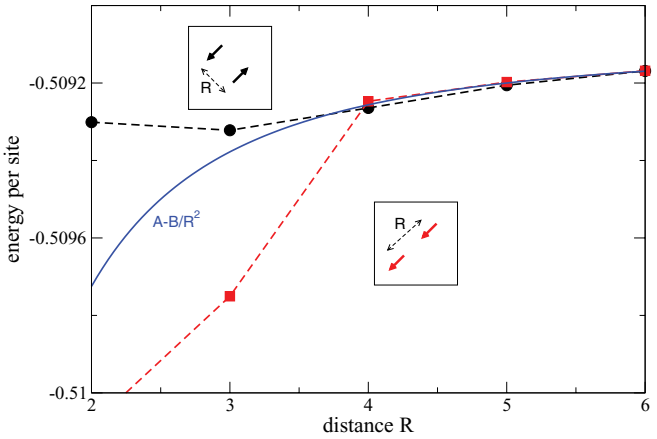


FIG. 2. (Color online) Energy of quadrupolar (circles, black) and head-to-tail alignment (diamonds, red) as a function of distance computed within the GA. For comparison the solid (blue) curve shows the dipole-dipole interaction Eq. (6) which approaches the GA result at large distances. Parameters for the GA computation: $U/t = 8, t'/t = -0.2$.

Figure 3 shows that segments formed by $N_c$ holes have systematically lower energy than $N_c$ spin polarons. Considering the segment as formed by $N_c/2$ VA pairs we obtain the binding energy $E_{\rm bind}$ between the pairs from $E(N_c) = E_2 N_c/2 + E_{\rm bind}(N_c/2 - 1)$, where $E_2$ is the energy of an isolated pair. Figure 3 reveals that the next-nearest-neighbor hopping $t'$ has a strong influence in determining the preferential orientation of the segments. Diagonal segments are more (less) stable than those oriented along the vertical or horizontal bond direction for small (large) values of $|t'/t|$ [see also inset to panel (b)]. Parameters appropriate for lanthanum cuprates ($t'/t \sim -0.15\ldots-0.2$)[40] yield a slight preference for diagonally oriented segments (11 direction) with respect to the vertical or horizontal directions.

In cuprate superconductors larger values of $|t'/t|$ are usually associated with the YBCO and multilayer materials. Indeed the observation of static incommensurate spin scattering in underdoped YBCO along the copper-oxygen bond direction is consistent with our computed segment orientation for larger $|t'/t|$.

Inclusion of a next-next-nearest-neighbor hopping $t''$ (with $t''/t > 0$) acts in the same direction as $t'/t < 0$; i.e., it further stabilizes horizontally (or vertically) over diagonally aligned segments. In addition we have checked that in the low-temperature orthorhombic (LTO) phase an anisotropy of $t'/t$ along orthorhombic $a$ and $b$ axes favors the orientation of the VA pairs along the $a$ axis.

## IV. EFFECT OF THE LONG-RANGE COULOMB INTERACTION

Until now we have neglected the long-range part of the Coulomb interaction which limits the infinite aggregation of VA pairs. In the spirit of considering the energy of charged clusters in a uniform compensating background,[43] we may estimate the effect of Coulomb interaction by considering $N_{\rm seg}$ segments, each composed of $N_c$ charges, embedded in a homogeneously charged background. For a fixed doping

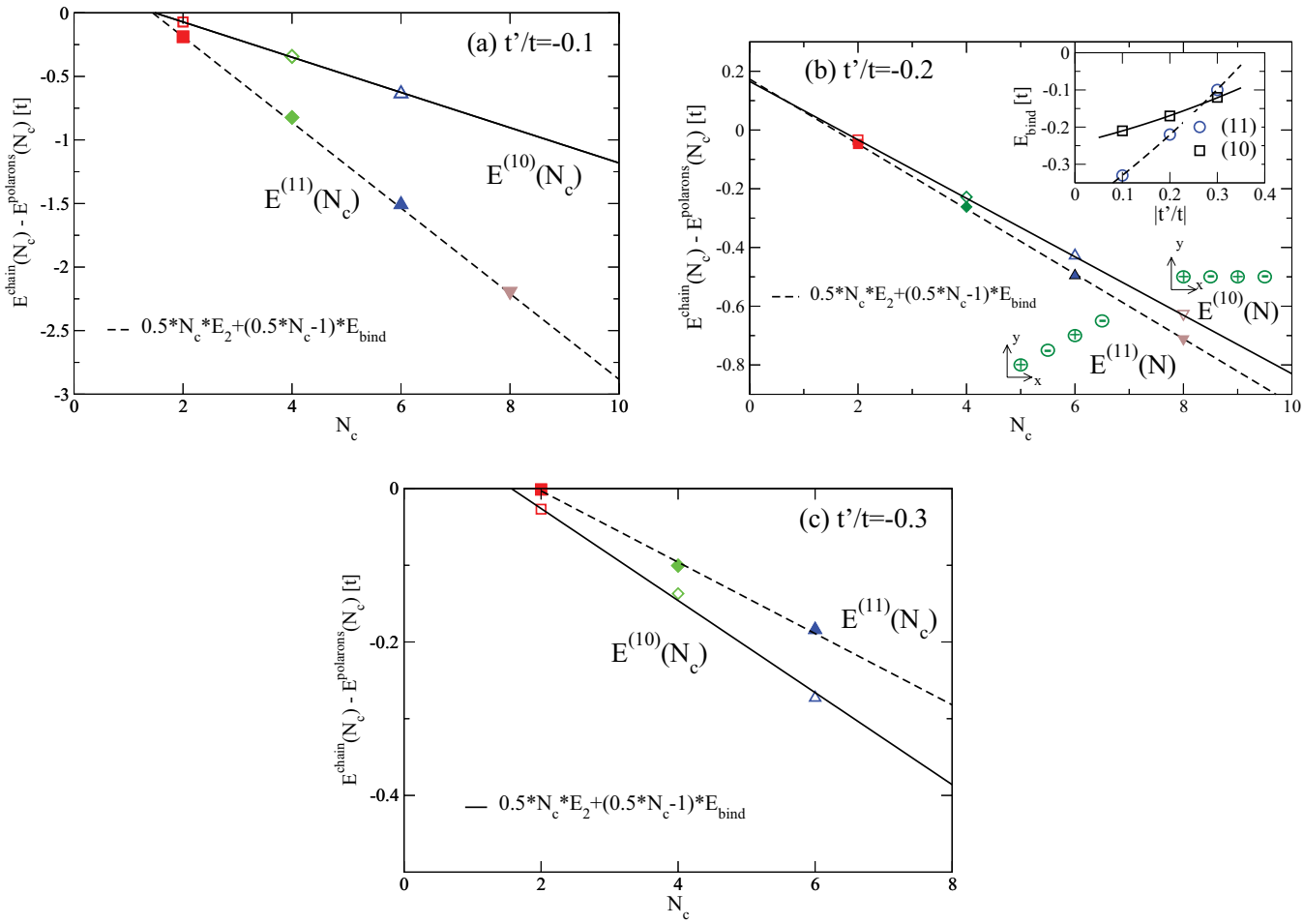


FIG. 3. (Color online) Energy of a chain of $N_c$ holes corresponding to $N_c/2$ VA pairs aligned along the vertical (open symbols, solid line) and diagonal direction (full symbols, dashed line) as compared to the energy of $N_c$ polarons. The slope of the lines corresponds to the binding energy between pairs. Parameters: $U/t = 8$, $t'/t = -0.1$ (a), $t'/t = -0.2$ (b), and $t'/t = -0.3$ (c) (with $t = 360$ meV in LSCO). The upper right inset to panel (b) shows the binding energy as a function of $t'/t$ for vertical (squares) and diagonal (circles) directions. Lines are guides to eyes. Computations were done in systems with up to $20 \times 20$ sites.

concentration $x = N_{\rm seg}N_c/L^2$ ($L^2$ being the number of sites) we want to estimate the optimum size of the segments allowing $N_c$ and $N_{\rm seg}$ to vary. For large $N_c$ the Coulomb energy per charge of each single segment increases logarithmically with the number of holes so the total energy reads

$$\frac{E(N_c)}{L^2} = x\left[\nu E_c \ln(N_c) + \gamma + \frac{1}{N_c}|E_{\rm bind}|\right] \qquad (7)$$

with $\gamma = (E_2 + E_{\rm bind})/2$ and $E_c = e^2/(\epsilon_0 a_{\rm ortho})$ a charging energy expressed in terms of the orthorhombic lattice constant $a_{\rm ortho}$ and of the static dielectric constant $\epsilon_0$. The filling factor $\nu$ is defined as the number of charges per site along the chain. The last term comprises the fact that shorter segments correspond to less total binding energy. The energy is minimized by $N_c = |E_{\rm bind}|/(\nu E_c)$ which leads to short segments of only few lattice constants at infinitesimal doping. However the above estimate is only a lower bound. Indeed Eq. (7) is valid if the Coulomb interaction between segments is neglected. To get a rough estimate of the intersegment Coulomb interaction in the dilute limit (when the length of a segment is much smaller than the segment separation) we consider in the Appendix the intersegment Coulomb energy estimated from a Wigner crystal of localized objects with charge $eN_c$.[44] In this case we find that the size of the segment even tends to increase with doping. Moreover, the log approximation of the energy of a single segment is not reliable for short segments. Including a suitable form of screened Coulomb interaction (see Appendix), we obtain $N_c \sim$ 2–10 depending on the chosen parameters.

## V. MAPPING TO A 2D SPIN MODEL

We assume that quenched disorder will yield a state in which segments have no positional order. We have checked numerically in an ensemble of segments[42] that the combination of long-range dipolar interaction plus short-range interaction favors a ferronematic alignment of the dipoles. An analogous state has been previously found for a two-component Fermi gas by Fregoso and Fradkin.[28]

Information on the spin response of a large aggregate of segments from the GA is hampered by the relatively small size of the clusters that can be numerically solved. Since the textures are planar and we are interested in the large-scale

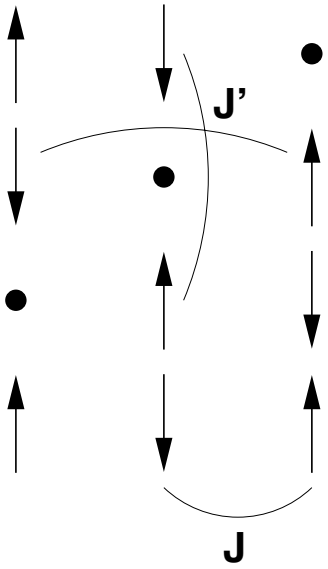


FIG. 4. Definition of couplings used in the $XY$-model calculation.

behavior, we consider instead a classical AF $XY$ model[45]

$$H = \sum_{ij} J_{ij}[S^x(\mathbf{r}_i)S^x(\mathbf{r}_j) + S^y(\mathbf{r}_i)S^y(\mathbf{r}_j)] \tag{8}$$

with antiferromagnetic $J_{ij} \equiv J$ interaction between nearest-neighbor sites $i,j$. The charge segments are modeled as a chain of vacancies which alternately correspond to the center of a vortex and antivortex of vorticity $\pm k$. In addition to the nearest-neighbor coupling $J$, we introduce an antiferromagnetic interaction $J'$ across the center of the (anti)vortices (see Fig. 4). $J'$ stabilizes the antiphase boundary of the segments and avoids the VA annihilation. The spin structure is then determined by minimizing the classical energy.

The angular spin distortion due to $N_{\rm seg}$ vortex-antivortex segments is given by considering the influence of a collection of $N_{\rm seg}$ equally oriented segments on spins at point $\mathbf{r}$:

$$\begin{aligned} S^x(\mathbf{r}) &= S_0 \exp(i\mathbf{Q}_{AF}\cdot\mathbf{r})\cos\Phi(\mathbf{r}), \\ S^y(\mathbf{r}) &= S_0 \exp(i\mathbf{Q}_{AF}\cdot\mathbf{r})\sin\Phi(\mathbf{r}), \end{aligned} \tag{9}$$

where $\mathbf{Q}_{AF} = (\pi,\pi)$ is the AF wave vector and the phase $\Phi(\mathbf{r})$ is the spin-velocity potential, whose gradient defines both the incommensurability and the spin current. We fix the value of $J'/J$ for the $XY$ model by comparing for a segment of two VA pairs the resulting charge and spin structure obtained from the GA [ Fig. 5(a)] and minimization of the $XY$-model energy [Fig. 5(b)]. Indeed we show in Fig. 6 that the spin phase for a diagonal cut through the segments shown in Fig. 5 coincides within the two approaches when $J'/J \sim 1$. Another parameter to fix is the filling factor $\nu$ introduced above. Whereas the site-centered VA chain shown in Fig. 1 has $\nu \approx 1$ there exists a similar plaquette-centered structure with comparable (though slightly higher) energy, which has $\nu \approx 0.65$. The filling factor of these structures is thus similar to those of (infinitely extended) diagonal site- and bond-centered stripes.[46] The following calculations assume $\nu = 0.7$. Note, however, that experimental data imply an increase toward larger $\nu$ close to the AF boundary.[18]

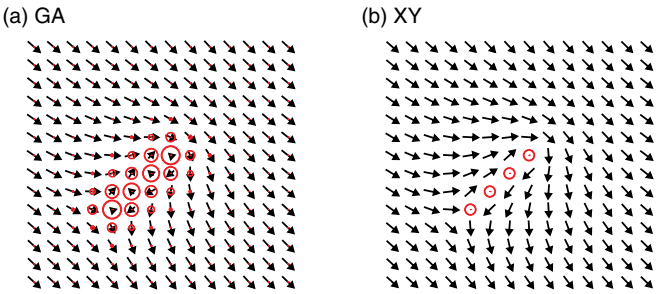


FIG. 5. (Color online) Segment of two vortex-antivortex pairs on a $14 \times 14$ lattice. (a) Gutzwiller approximation of the Hubbard model with $U/t = 8$, $t'/t = -0.2$. (b) $XY$ model with $J'/J = 1$. In (a) the radius of the circles indicates the (hole) charge density and in (b) corresponds to an empty site.

Figure 7(a) reports the spin phase distribution on a lattice of $160 \times 160$ sites for a particular random distribution of stripe dipoles with segment length of 8 sites at $x = 0.03$, all polarized along the $[-1,1]$ direction. One observes a monotonic increase on the phase of the staggered magnetization along the $[1,1]$ direction, which will lead to the incommensurate modulation of the spin response. In Fig. 7(b), for the same distribution of segments, the associated dipole orientation is now completely random. Contrary to the case of Fig. 7(a), the system now disaggregates into large areas with similar phase. As already stated, the short-range contribution to the dipole-dipole interaction favors the ferromagnetic alignment [i.e., the configuration Fig. 7(a) is energetically more stable than Fig. 7(b)].

The numerical results can be understood by considering the long-range phase distortion produced by the segments.[47] The total phase change $\Phi(\mathbf{r})$ of Eqs. (9) given by the angular spin distortion due to the $N_{\rm seg}$ segments with V and A of vorticity $\pm k$ centered at $z_{i,\pm}$ ($\mathbf{r}_{i,\pm}$) can be expressed by mapping the Cartesian plane into the complex plane $(x,y) \to z = x + iy$,

$$\Phi(z) = k\ \mathrm{Im} \sum_{i=1}^{N_c N_{\rm seg}/2} [\ln(z - z_{i,-}) - \ln(z - z_{i,+})]. \tag{10}$$

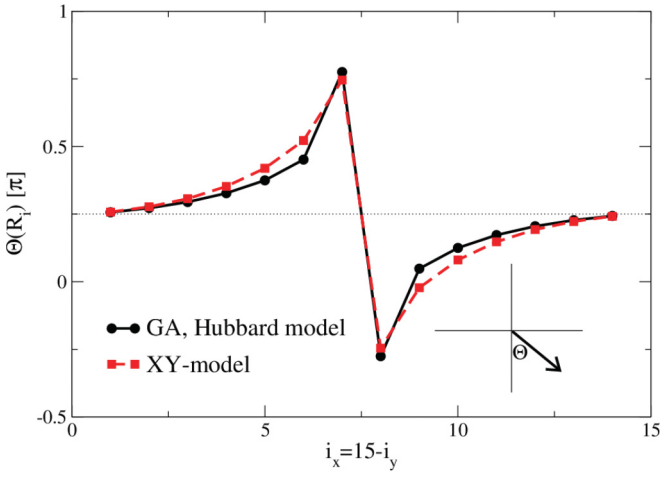


FIG. 6. (Color online) Spin phase for a diagonal cut through the segments shown in Fig. 5.

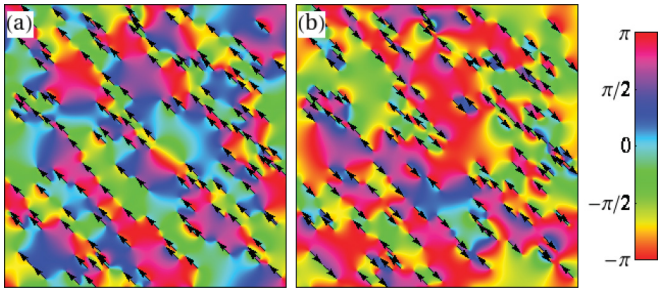


FIG. 7. (Color online) Spin phase distribution for (a) macroscopically and (b) randomly polarized distribution of stripe dipoles in a 160×160 site system. Segments have a length of 8 sites on the diagonal (4 VA pairs) and are represented by arrows indicating the length and polarization. With a filling factor $\nu = 0.7$ the total number of segment sites corresponds to a doping of $x = 0.03$.

For one segment with "dipole moment" $\boldsymbol{\mu}_{\rm seg}$ we obtain by direct integration that the average spin current in the direction perpendicular to the segment is $\langle \nabla\Phi(\mathbf{r})\rangle_{\rm seg} = \pi \boldsymbol{\mu}_{\rm seg} \times \hat{z}/(La_{\rm tetra})^2$, where we explicitly introduced the tetragonal lattice constant $a_{\rm tetra}$ and with $\hat{z}$ pointing out of the plane. $La_{\rm tetra}$ denotes the linear dimension of the system. The separation of vortex and antivortex at the extremes of the (diagonal) segment determines the length of the dipole segments, while the vorticity $k$ has to be replaced by an effective vorticity $k_{\rm eff} < 1$ to be determined numerically. The strength of the dipole moment is then given by $|\boldsymbol{\mu}_{\rm seg}| = k_{\rm eff} a_{\rm ortho} N_c/\nu$ and the numerical calculation yields $k_{\rm eff}/\nu \sim 2$. The macroscopic spin current for $N_{\rm seg}$ equally oriented segments is thus given by $\nabla\Phi(\mathbf{r})_{\rm mac} = \pi \hat{z} \times \mathbf{P}$ where $\mathbf{P}$ is the macroscopic polarization in the charge analogy $\mathbf{P} = \boldsymbol{\mu}_{\rm seg} N_{\rm seg}/(La_{\rm tetra})^2$. Clearly $\mathbf{P}$ plays the role of the ferronematic order parameter. From Eq. (9) one obtains that the macroscopic spin current implies an incommensurate spin response perpendicular to the segments with $\mathbf{q} = \nabla\Phi(\mathbf{r})_{\rm mac}$. One thus finds a linear dependence of the incommensurability on doping

$$q_\perp = \sqrt{2}\pi \frac{k_{\rm eff}}{\nu} \frac{1}{a_{\rm tetra}} x \equiv \pi P_\perp \tag{11}$$

with $a_{\rm ortho} = \sqrt{2} a_{\rm tetra}$.

Equation (11) relates the incommensurability to the ferronematic order parameter and is one of our central results. This linear relation between incommensurability and doping is similar to the linear relation found for ordered stripe arrays at low doping.[8,50] Thus experimentally the two phases are not easily distinguished in the magnetic channel and the main difference will arise in the charge channel with equally spaced stripes producing Bragg peaks in contrast to diffusive scattering in the case of segments.

For a set of configurations of macroscopically polarized VA segments on a lattice of 160 × 160 sites as shown in Fig. 7(a) we now evaluate the magnetic neutron cross section

$$\frac{d\sigma}{d\Omega dE} \sim \sum_{\alpha\beta} (\delta_{\alpha\beta} - \hat{q}_\alpha \hat{q}_\beta) S^\alpha(\boldsymbol{q}) S^\beta(\boldsymbol{q})$$

for different dopings. Our results are compared in Fig. 8 with elastic neutron scattering data from Ref. 17. The specific scattering geometry [Fig. 2(b) of Ref. 17] which is composed

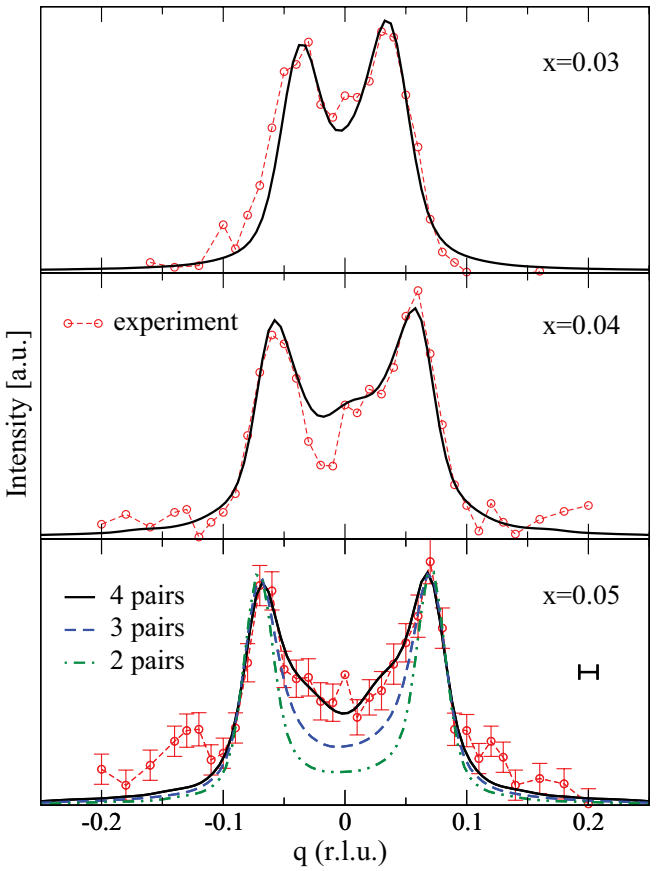


FIG. 8. (Color online) Fits of the spin structure factor (LSCO) at different dopings for $N_c = 8$ segments as explained in the text. For $x = 0.05$ we also show spectra for $N_c = 4,6$ segments for comparison. Computations have been done on lattices with up to 160 × 160 sites and we average over 20–30 segment configurations where the experimental resolution (horizontal bar in the lower panel; cf. Fig. 4 of Ref. 17) has been taken into account by convoluting with a Gaussian. The trajectory of the momentum scan is labeled as (a) in Fig. 4 of Ref. 17. Data by courtesy of S. Wakimoto.

of two twin domains with population 2 : 1 has been taken into account. This gives rise to the asymmetry of the spectra since $Q_{AF}$ of the B twin does not coincide with $Q_{AF}$ of the A twin.[51] The incommensurate peak position $q_c$ is independent from the segment size as expected from Eq. (11). On the other hand the size influences the peak width as can be seen in the lowest panel of Fig. 8. By decreasing the dipole moment $\mu_{\rm seg}$ at fixed doping, the increasing number of segments decreases the fluctuations of the dipole polarization. The strength of the incommensurate response is then favored with respect to the commensurate one. As can be seen from Fig. 8 one finds excellent agreement with the experimental data for segments with 4 VA pairs (i.e., 8 sites) whereas shorter segments underestimate the intensity at $Q_{AF}$ (see lower panel of Fig. 8).

## VI. DISCUSSION OF THE RESULTS

The excellent agreement of the spin structure in the ferronematic state with neutron scattering experiments could also account for the composite spin response at $x \leqslant 0.02$ in LSCO. Upon reducing doping below $x = 0.02$ in the Néel

state, this system displays a coexistence of commensurate spin order and incommensurate spin scattering, with the spin incommensurability wave vector saturating at the value attained at $x = 0.02$.[20] This observation clearly points toward a phase separation and according to our present analysis the VA segments tend to segregate from the commensurate AF phase with a volume fraction proportional to the doping $x$.

The macroscopic constant spin current can be considered as an average spiral behavior of the spins. In this sense our theory has some similarity with the proposal of Ref. 2. However, the state emerging from our analysis is different in many respects. First of all we find that in the absence of pinning potentials the charge organizes forming rather long segments (6–10 carriers in the $x = 0.03$–$0.05$ doping range of LSCO), which might be the seeds for the formation of the stripes observed at higher dopings. Of course when the pinning potential due to the out-of-plane impurities dominates, the segments are disrupted because its constituents are attracted around each Sr impurity. However, the rather large dielectric constant of LSCO, the relatively large impurity density (at distances smaller than 6–8 lattice spacings for $x = 0.03$), and their out-of-plane location conspire to produce a rather smooth potential landscape on the planes, which suggests that the aggregation tendency might be dominant and longer segments should be considered. Of course the smooth quenched disorder landscape still provides a pinning source for the charge segments thereby disrupting any segment positional order. Another difference with respect to Ref. 2 is that in our scenario topological spin textures are present at each extreme of the charge segments producing the spin spiral state with the ferronematic order. Therefore in the present case the spiral spin state is a collective effect, which is slaved by the ferronematic order of the stripe segments.

As shown in the inset to Fig. 3 $|E_{\rm bind}|$ decreases with increasing $|t'/t|$; the reduction is, however, more pronounced for diagonal VA pairs. This results in a crossing of the alignments as a function of $N_c$ for $-0.3 < t'/t < -0.2$. In addition the lattice structure can influence the orientation. This explains the fact that a diagonal incommensurate spin response has only been observed in nonsuperconducting underdoped lanthanum cuprates where $|t'/t|$ is small[40] and which display a LTO structure in the underdoped regime. At higher doping an increased fraction of local octahedral tilts with LTT symmetry[52] may drive a reorientation of the stripe segments from diagonal to the copper-oxygen direction at the insulator metal transition $x \approx 0.05$. It is also worth mentioning that the similarity of the incommensurability of low-energy spin fluctuations observed for $Bi_{2+x}Sr_{2-x}CuO_{6+y}$ (Bi2201)[21] with that of LSCO includes the rotation towards the diagonal direction for strong underdoping. For this compound the value of $t'/t$ has been estimated in Ref. 53 to be similar to LSCO (at least in the underdoped regime). Therefore the formation of VA segments and the induced spin incommensurability is also expected to be similar in LSCO and Bi2201 materials. In $Bi_2Sr_2CaCu_2O_{8+y}$ compounds where $t'/t$ is large[40] we expect alignment of the segments along the Cu-O direction resulting in an inequivalence of hole density on the corresponding $x$ and $y$ oxygen sites. It therefore would be interesting to investigate whether this feature can account for the intra-unit-cell nematicity observed by scanning tunneling microscopy[54] in these materials.

Apart from the excellent agreement found for the spin structure factor other facts point to the correctness of our interpretation. As far as transport is concerned, resistivity anisotropy has been found in strongly underdoped LSCO and YBCO, which directly indicate the breaking of $C_4$ rotational symmetry.[55] The absence of a simultaneous breaking of translational invariance indicates that a nematic state is likely formed in the insulating phase of these systems. The self-organization of charges at low temperature also entails an activated or variable-range-hopping behavior, which should become weaker upon increasing doping, when the segment length and density increases together with the screening and the eventual appearance of quasiparticles in the metallic state at $x \gtrsim 0.055$. The charge self-organization might also survive in the metallic region giving rise to two-component phases[56] of coexisting quasiparticles and segments. How this state evolves into the stripe state is an interesting question, which deserves investigations outside the scope of the present work.

We expect that thermal fluctuations will disorder the dipole orientation reducing the order parameter until a thermodynamic phase transition occurs. It is not clear whether the high-temperature state will be only nematic as in Fig. 7(b) with a second transition at higher temperature to an isotropic state of fully disordered dipoles or if the transition will be directly to the isotropic state. In both cases the incommensurability should display an order parameter behavior. In agreement with this expectation, an order-parameter-like temperature dependence of the incommensurability has already been noticed in YBCO.[22,23]

Since the ferronematic state breaks inversion symmetry one expects on general grounds[57] that it will lead to a real ferroelectric distortion, i.e., to become multiferroic through, e.g., the inverse Dzyaloshinskii-Moriya mechanism.[58] Indeed, a ferroelectric state has recently been detected in strongly underdoped lanthanum cuprates.[59] Unfortunately, a small number of free carriers will make the effect undetectable with capacitance measurements which may explain why it has been seen only at very low temperatures. An appealing possibility would be to look for inversion-symmetry breaking with second-harmonic generation (SHG) which does not require perfect insulating behavior.[60] We expect that the SHG signal as a function of temperature tracks the incommensurability.

Concluding, we have proposed a phase for strongly underdoped cuprates which breaks $C_4$ rotational and inversion symmetry. Our theory provides a consistent explanation for the elastic incommensurate response seen by magnetic neutron scattering experiments and reconciles it with the lacking signatures of charge order. It remains to be seen how the nematic segments act as seeds which lead to smectic correlations (stripes) in some of the cuprate materials.

## ACKNOWLEDGMENTS

We thank S. Caprara, R. De Renzi, S. Sanna, and P. Carretta for insightful discussions and S. Wakimoto for sending to us the data shown in Fig. 8. J.L. is supported by Italian Institute of Technology Seed Project NEWDFESCM. G.S. acknowledges support from the Deutsche Forschungsgemeinschaft. M.G. acknowledge financial support from University Research Project of Sapienza University No. C26A115HTN.

## APPENDIX: INFLUENCE OF LONG-RANGE COULOMB INTERACTION

Suppose we have $N$ holes and we want to find the optimum way to accommodate them in $N_s$ segments each one accommodating $N_c$ holes. Obviously $N = N_s N_c$ and the question is whether we should choose few long segments or many short segments.

To solve this problem we use the energies obtained from the minimization of the GA energy functional for chains with different number of VA pairs (see Fig. 3). The energy to add a pair is $\epsilon_{VA} = E(1VA) - E_{AF}$. If the pairs are far from each other the energy of $N_{VA}$ pairs is $E(N_{VA}) = N\epsilon_{VA} + E_{AF}$. On the other hand, if the pairs form a chain the energy becomes

$$E(N_{VA}) = N\epsilon_{VA} + E_{AF} + (N_{VA} - 1)E_{\rm bind}.$$

Since polaron states are more stable then isolated vortices it is convenient to subtract the energy of $2N_{VA}$ separated polarons $[\epsilon_p = E(1p) - E_{AF}]$ which yields

$$E(N_{VA}) - E_{\rm pol}(2N_{VA}) = N_{VA}(\epsilon_{VA} - 2\epsilon_p) + (N_{VA} - 1)E_{\rm bind}$$

and corresponds to the quantity we plot in Figs. 3. Putting $N_{VA} = N_c/2$ and $\gamma = (\epsilon_{VA} - 2\epsilon_p + E_{\rm bind})/2$, the energy of one segment is then $E(N_c) = \gamma N_c - E_{\rm bind}$.

### 1. Isolated segments

We first consider segments which are far apart and thus include only the intra-segment long-range Coulomb energy

$$V_{\rm coul} = \frac{e^2}{2\epsilon_0 a_{\rm ortho}} \sum_{n\neq m} \frac{1}{|n-m|} = \frac{e^2 N_c}{2\epsilon_0 a_{\rm ortho}} \sum_{n=1}^{N_c} \frac{1}{n}$$
$$\approx \frac{e^2 N_c}{2\epsilon_0 a_{\rm ortho}} \ln(N_c),$$

where we made an asymptotic expansion of the harmonic series for large $N_c$.

If we have $N_s$ segments which are far apart the total energy, including the Coulomb self-energy, is then

$$E = N_s[N_c E_c \ln(N_c) + N_c\gamma - E_b]$$

with $E_c = e^2/4\pi\epsilon_0\epsilon_r a_{\rm ortho}$. Using the constraint $N = N_s N_c$ and defining $x = N/L^2$ one obtains

$$\frac{E}{L^2} = x\left[E_c \ln(N_c) + \gamma + \frac{1}{N_c}|E_{\rm bind}|\right]. \quad \text{(A1)}$$

The last term is the "surface" energy cost due to the cutting of segments and the minimum of $E/L^2$ is obtained for

$$N_c = \frac{|E_{\rm bind}|}{E_c}.$$

For $a_{\rm ortho} \approx 5$ Å and an in-plane dielectric constant of $\epsilon_\parallel \approx 30$ one arrives at $E_c \approx 0.1$ eV $\approx 0.3t$ which is of the same magnitude as the binding energy evaluated in our paper. In order to get a better estimate for short segment lengths (where the log approximation of the harmonic series breaks down) we use in Eq. (A1) the form of the long-range part, which was previously used in Ref. 61,

$$V(\mathbf{r}) = \frac{V_0 e^{-|\mathbf{r}|/\lambda}}{\sqrt{\mathbf{r}^2 + \alpha^2}}, \quad \text{(A2)}$$

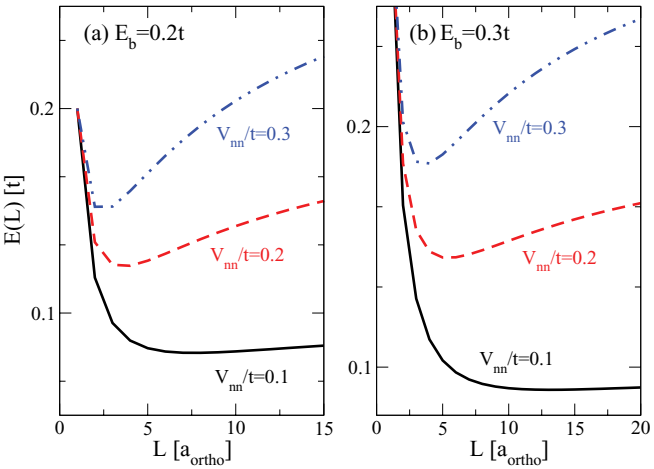


FIG. 9. (Color online) Energy per charge $E(L) = [V_{\rm coul}(L) - E_{\rm bind}]/N_c$ as a function of segment length $L$ evaluated with the Coulomb interaction Eq. (A2). Binding energy $E_{\rm bind}/t = 0.2$ (a) and $E_{\rm bind}/t = 0.3$ (b). Screening length $\lambda = 20a_{\rm ortho}$.

and compute the energy minimum numerically. The parameters $V_0$ and $\alpha$ are fixed by the on-site $[V(0) = U/4]$ and nearest-neighbor repulsion $[V(a) \equiv V_{nn}]$. Figure 9 shows the resulting energy per charge as a function of segment length for binding energy $E_{\rm bind}/t = 0.2$ and $E_{\rm bind}/t = 0.3$, respectively. The estimate thus supports the stability of segments with length $L = 2\ldots 10a_{\rm ortho}$ depending on parameters.

### 2. Long-range interaction between segments

The result above is valid if the segments are far apart. However, as the segments become closer the interaction energy between them becomes important which can be estimated in close analogy to the evaluation of the Wigner crystal.[44]

In the low-density limit, the energy per segment (charge $Q$) of a "Wigner solid" is given by

$$\frac{E_W}{N_s} = \frac{Q^2}{2a_B}\left[-\frac{\alpha}{r_s} + \frac{\beta}{r_s^{3/2}} + \cdots\right], \quad \text{(A3)}$$

where $a_B = \hbar^2/(mQ^2)$ denotes the Bohr radius and $r_s = r_0/a_B$, with $r_0$ defined from the volume per segment $L^{\mathcal{D}}/N_s = r_0^{\mathcal{D}}$ in $\mathcal{D}$ dimensions. The coefficients $\alpha, \beta$ are of order unity and have been derived for the two- and three-dimensional Wigner solid in Refs. 62 and 63.

Each of the segments consists of $N_c$ charges (charge $e$), i.e., $Q = N_c e$, and the total number of charges is given by $N = N_s N_c$. The Wigner energy becomes

$$E_W = N_s N_c^4 \frac{e^2}{2a_0}\frac{1}{r_s}\left[-\alpha + \frac{\beta}{r_s^{1/2}}\right] \quad \text{(A4)}$$

with $a_0 = \hbar^2/(me^2)$. Furthermore one has

$$r_s^{\mathcal{D}} = \left(\frac{r_0 N_c^2}{a_0}\right)^{\mathcal{D}} = \frac{L^{\mathcal{D}}}{N_s}\left(\frac{N_c^2}{a_0}\right)^{\mathcal{D}} = \frac{N_c}{x}\left(\frac{N_c^2}{a_0}\right)^{\mathcal{D}}, \quad \text{(A5)}$$

where we have introduced doping $x = N/L^{\mathcal{D}}$.

Inserting Eq. (A5) into Eq. (A4) yields

$$\frac{E_W}{L^{\mathcal{D}}} = \frac{e^2}{2} x^{1+1/\mathcal{D}} N_c^{1-1/\mathcal{D}} \left[ -\alpha + \beta \frac{\sqrt{a_0}}{N_c} \left( \frac{x}{N_c} \right)^{1/(2\mathcal{D})} \right]. \quad \text{(A6)}$$

Adding the energy Eq. (A1) for the formation of the individual segments one finally has in the two-dimensional case

$$\frac{E}{L^2} = x E_c \left\{ \frac{\gamma}{E_c} + \ln(N_c) + \frac{1}{N_c} \frac{|E_{\text{bind}}|}{E_c} - \frac{\alpha}{2} \sqrt{x N_c} + \mathcal{O}\left[ \left( \frac{x}{N_c} \right)^{3/4} \right] \right\}, \quad \text{(A7)}$$

which shows that an infinitesimal Wigner contribution completely changes the picture. The energy has two minima, one at finite $N_c$ and the other at infinite $N_c$ as the square root dominates the energy. Essentially, the previous solution becomes metastable and a lower energy solution arises with negative divergent energy. Of course, once $N_c$ tends to diverge it is not any longer correct to compute the energy in the Wigner way and one needs to consider the Coulomb interaction between large segments which will cut off the energy.

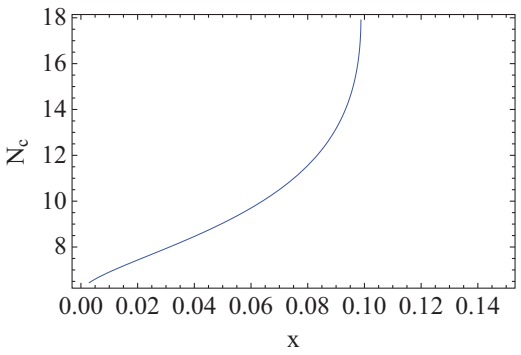


FIG. 10. (Color online) Optimum $N_c$ for the metastable solution for $|E_{\text{bind}}|/E_c = 6$ and $\alpha = 2$.

It is interesting that there is a critical value of the doping at which the metastable short segment solution disappears (see Fig. 10). It is worth investigating in future work whether this indicates a transition from short segments to infinite stripes.


[1] C. M. Varma, Phys. Rev. Lett. **83**, 3538 (1999).
[2] O. P. Sushkov and V. N. Kotov, Phys. Rev. Lett. **94**, 097005 (2005).
[3] L. Benfatto, S. Caprara, and C. Di Castro, Eur. Phys. J. B **17**, 95 (2000).
[4] C. Nayak, Phys. Rev. B **62**, 4880 (2000).
[5] W. Metzner, D. Rohe, and S. Andergassen, Phys. Rev. Lett. **91**, 066402 (2003).
[6] U. Löw, V. J. Emery, K. Fabricius, and S. A. Kivelson, Phys. Rev. Lett. **72**, 1918 (1994).
[7] C. Castellani, C. Di Castro, and M. Grilli, Phys. Rev. Lett. **75**, 4650 (1995).
[8] J. Zaanen and O. Gunnarsson, Phys. Rev. B **40**, 7391 (1989).
[9] K. Machida, Physica C **158**, 192 (1989).
[10] M. Raczkowski, M. Capello, D. Poilblanc, R. Frésard, and A. M. Oleś, Phys. Rev. B **76**, 140505 (2007).
[11] P. Abbamonte, A. Rusydi, S. Smadici, G. D. Gu, G. A. Sawatzky, and D. L. Feng, Nat. Phys. **1**, 155 (2005).
[12] J. Fink, E. Schierle, E. Weschke, J. Geck, D. Hawthorn, V. Soltwisch, H. Wadati, H.-H. Wu, H. A. Dürr, N. Wizent, B. Büchner, and G. A. Sawatzky, Phys. Rev. B **79**, 100502 (2009).
[13] J. M. Tranquada, B. J. Sternlieb, J. D. Axe, Y. Nakamura, and S. Uchida, Nature (London) **375**, 561 (1995).
[14] G. Ghiringhelli, M. Le Tacon, M. Minola, S. Blanco-Canosa, C. Mazzoli, N. B. Brookes, G. M. De Luca, A. Frano, D. G. Hawthorn, F. He, T. Loew, M. Moretti Sala, D. C. Peets, M. Salluzzo, E. Schierle, R. Sutarto, G. A. Sawatzky, E. Weschke, B. Keimer, and L. Braicovich, Science **337**, 821 (2012).
[15] J. Chang, N. Doiron-Leyraud, O. Cyr-Choinière, G. Grissonnanche, F. Laliberté, E. Hassinger, J-Ph. Reid, R. Daou, S. Pyon, T. Takayama, H. Takagi, and L. Taillefer, Nat. Phys. **8**, 751 (2012).
[16] S. Wakimoto, G. Shirane, Y. Endoh, K. Hirota, S. Ueki, K. Yamada, R. J. Birgeneau, M. A. Kastner, Y. S. Lee, P. M. Gehring, and S. H. Lee, Phys. Rev. B **60**, R769 (1999).
[17] S. Wakimoto, R. J. Birgeneau, M. A. Kastner, Y. S. Lee, R. Erwin, P. M. Gehring, S. H. Lee, M. Fujita, K. Yamada, Y. Endoh, K. Hirota, and G. Shirane, Phys. Rev. B **61**, 3699 (2000).
[18] M. Matsuda, M. Fujita, K. Yamada, R. J. Birgeneau, M. A. Kastner, H. Hiraka, Y. Endoh, S. Wakimoto, and G. Shirane, Phys. Rev. B **62**, 9148 (2000).
[19] K. Yamada, C. H. Lee, K. Kurahashi, J. Wada, S. Wakimoto, S. Ueki, H. Kimura, Y. Endoh, S. Hosoya, G. Shirane, R. J. Birgeneau, M. Greven, M. A. Kastner, and Y. J. Kim, Phys. Rev. B **57**, 6165 (1998).
[20] M. Matsuda, M. Fujita, K. Yamada, R. J. Birgeneau, Y. Endoh, and G. Shirane, Phys. Rev. B **65**, 134515 (2002).
[21] M. Enoki, M. Fujita, T. Nishizaki, S. Iikubo, D. K. Singh, S. Chang, J. M. Tranquada, and K. Yamada, arXiv:1205.3301.
[22] V. Hinkov, D. Haug, B. Fauqué, P. Bourges, Y. Sidis, A. Ivanov, C. Bernhard, C. T. Lin, and B. Keimer, Science **319**, 597 (2008).
[23] D. Haug, V. Hinkov, Y. Sidis, P. Bourges, N. B. Christensen, A. Ivanov, T. Keller, C. T. Lin, and B. Keimer, New J. Phys. **12**, 105006 (2010).
[24] R. Daou, J. Chang, David LeBoeuf, Olivier Cyr-Choinière, Francis Laliberté, Nicolas Doiron-Leyraud, B. J. Ramshaw, Ruixing Liang, D. A. Bonn, W. N. Hardy, and L. Taillefer, Nature (London) **463**, 519 (2010).
[25] S. A. Kivelson, E. Fradkin, and V. J. Emery, Nature (London) **393**, 550 (1998).
[26] M. Vojta, Adv. Phys. **58**, 699 (2009).
[27] K. Sun, M. J. Lawler, and E.-A. Kim, Phys. Rev. Lett. **104**, 106405 (2010).
[28] B. M. Fregoso and E. Fradkin, Phys. Rev. Lett. **103**, 205301 (2009).
[29] J. A. Vergés, E. Louis, P. S. Lomdahl, F. Guinea, and A. R. Bishop, Phys. Rev. B **43**, 6099 (1991).
[30] G. Seibold, Phys. Rev. B **58**, 15520 (1998).
[31] M. Berciu and S. John, Phys. Rev. B **69**, 224515 (2004).
[32] H. Koizumi, J. Phys. Soc. Jpn. **77**, 034712 (2008).

[33]C. Timm and K. H. Bennemann, Phys. Rev. Lett. **84**, 4994 (2000).
[34]F. Gebhard, Phys. Rev. B **41**, 9452 (1990).
[35]G. Kotliar and A. E. Ruckenstein, Phys. Rev. Lett. **57**, 1362 (1986).
[36]J. Lorenzana and G. Seibold, Low Temp. Phys. **32**, 320 (2006).
[37]G. Seibold and J. Lorenzana, Phys. Rev. Lett. **94**, 107006 (2005).
[38]J. Lorenzana, G. Seibold, and R. Coldea, Phys. Rev. B **72**, 224511 (2005).
[39]L. F. Feiner, J. H. Jefferson, and R. Raimondi, Phys. Rev. Lett. **76**, 4939 (1996).
[40]E. Pavarini, I. Dasgupta, T. Saha-Dasgupta, O. Jepsen, and O. K. Andersen, Phys. Rev. Lett. **87**, 047003 (2001).
[41]T. Tlasty and S. A. Sofran, Science **290**, 1328 (2000).
[42]M. Capati, G. Seibold, C. Di Castro, M. Grilli, and J. Lorenzana, (unpublished).
[43]J. Lorenzana, C. Castellani, and C. Di Castro, Europhys. Lett. **57**, 704 (2002); Phys. Rev. B **64**, 235127 (2001).
[44]E. P. Wigner, Trans. Farad. Soc. **34**, 678 (1938).
[45]P. M. Chaikin and T. C. Lubensky, *Principles of Condensed Matter Physics* (Cambridge University Press, 2000).
[46]G. Seibold and J. Lorenzana, Phys. Rev. B **80**, 012509 (2009).
[47]In this regard it is useful to remember that a vortex in an *XY* spin system in two dimensions can be mapped to a 2D Coulomb charge (Ref. 48) or alternatively to current wires perpendicular to the 2D plane. The sign of the charges or the direction of the current is then determined by the vorticity. Thus the VA pairs map into 2D electric dipoles in the Coulomb analogy or 2D magnetic dipoles perpendicular to the former in the current analogy. In the latter case the magnetic field maps into the spin current which will be used below. Using this magnetic analogy and standard arguments from the theory of macroscopic dielectrics and magnetized systems (Ref. 49) it is easy to see that the system develops a macroscopic "magnetic field" equivalent to an average net spin current perpendicular to the segments' orientation and proportional to the average polarization.
[48]P. Minnhagen, Rev. Mod. Phys. **59**, 1001 (1987).
[49]J. D. Jackson, *Classical Electrodynamics* (Wiley, New York, 1998).
[50]J. Lorenzana and G. Seibold, Phys. Rev. Lett. **89**, 136401 (2002).
[51]For the experimental data in Fig. 8 this feature may be masked by the error bars but the effect is clearly visible, e.g., in Fig. 1(b) of Ref. 18.
[52]E. S. Bozin, S. J. L. Billinge, G. H. Kwei, and H. Takagi, Phys. Rev. B **59**, 4445 (1999).
[53]M. Hashimoto, T. Yoshida, H. Yagi, M. Takizawa, A. Fujimori, M. Kubota, K. Ono, K. Tanaka, D. H. Lu, Z. X. Shen, S. Ono, and Y. Ando, Phys. Rev. B **77**, 094516 (2008).
[54]M. J. Lawler, K. Fujita, Jhinhwan Lee, A. R. Schmidt, Y. Kohsaka, Chung Koo Kim, H. Eisaki, S. Uchida, J. C. Davis, J. P. Sethna, and Eun-Ah Kim, Nature (London) **466**, 347 (2010).
[55]Y. Ando, K. Segawa, S. Komiya, and A. N. Lavrov, Phys. Rev. Lett. **88**, 137005 (2002).
[56]Y. Ando, Y. Kurita, S. Komiya, S. Ono, and K. Segawa, Phys. Rev. Lett. **92**, 197001 (2004).
[57]M. Mostovoy, Phys. Rev. Lett. **96**, 067601 (2006).
[58]I. A. Sergienko and E. Dagotto, Phys. Rev. B **73**, 094434 (2006).
[59]Z. Viskadourakis, I. Radulov, A. P. Petrović, S. Mukherjee, B. M. Andersen, G. Jelbert, N. S. Headings, S. M. Hayden, K. Kiefer, S. Landsgesell, D. N. Argyriou, and C. Panagopoulos, Phys. Rev. B **85**, 214502 (2012).
[60]M. Fiebig, J. Phys. D **38**, R123 (2005).
[61]G. Seibold, C. Castellani, C. Di Castro, and M. Grilli, Phys. Rev. **58**, 13506 (1998).
[62]W. J. Carr Jr., Phys. Rev. **122**, 1437 (1961).
[63]L. Bonsall and A. A. Maradudin, Phys. Rev. B **15**, 1959 (1977).